Contribution of the breathing modes in the SWTBLI unsteadiness

Ismaïl Ben Hassan Saïdi, Guillaume Fournier, Christian Tenaud

Association Aéronautique et Astronautique de France

55th 3AF International Conference on Applied Aerodynamics
23 — 25 March 2020, Poitiers – France

FPnum-AERO2020-name

Contribution of the breathing modes in the SWTBLI unsteadiness

Ismaïl BEN HASSAN SAÏDI[(1)]*and Guillaume FOURNIER Author[(2)] and Christian TENAUD[(3)] †

[(1)]*Université Paris-Saclay, CNRS, LIMSI, 91405, Orsay, France, ismail.ben-hassan-saidi@limsi.fr*

[(2)]*Université Paris-Saclay, Univ Evry, LMEE, 91020, Evry, France, guillaume.fournier@ufrst.univ-evry.fr*

[(3)]*Université Paris-Saclay, CNRS, LIMSI, 91405, Orsay, France, christian.tenaud@centralesupelec.fr*

ABSTRACT

The physical origin of strong Shock Wave Boundary Layer Interaction (SWBLI) low frequency unsteadiness is still unclear. It has been related either to the shedding of vortices in the mixing layer downstream of the separation, or to the turbulent structures in the incoming boundary layer. The aim of the present work is to perform well resolved DNS of SWBLISs and analyse results in order to contribute to a better understanding of the SWBLI unsteadiness and the physical mechanism causing these low frequency oscillations. First, the interaction involving a laminar incoming boundary layer is simulated in order to suppress the suspected influence of the large turbulent structures of the boundary layer on the SWBLI unsteadiness. The simulation of the fully turbulent case is then presented. The comparison between the two flows pleads for an origin of the SWBLI unsteadiness associated to the low frequency dynamics of the separated zone.

1. INTRODUCTION

Situations where an incident shock wave impinges upon a boundary layer are commonly encountered in the aeronautical and the aerospace industries. For instance, it possibly occurs in flows around an aircraft in supersonic flight, in turbojets, in supersonic air intakes or in rocket nozzles. In a shock wave boundary layer interaction (SWBLI), if the shock wave is strong enough (strong interaction), the compression of the flow can lead to the separation of the boundary layer. A recirculation bubble is then created surrounded by a complex system of multiple shock waves. The steady organization of such flow is presented in figure 1 for the well documented configuration of the interaction between an incident oblic shock wave impinging a boundary layer developing on a flat plate.

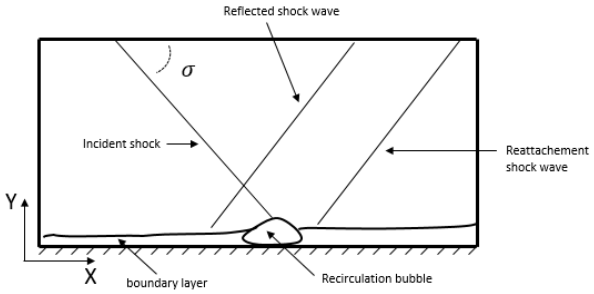

Figure 1: Sketch of the flow.

The steady organization of the flow presented in figure 1 corresponds to the mean organization of the flow. The dynamical features of the SWBLI are characterized by several unsteady phenomena whose characteristic scales spread over a large broadband spectrum range. In general, the incoming boundary layer is not laminar and the turbulent activity of the boundary layer exhibits a large kinetic energy spectrum with a characteristic Strouhal number $S_\delta = \frac{f\delta}{U_e} \sim 1$ (where f, δ and U_e are respectively the characteristic frequency of the fluctuations, the boundary layer thickeness before the interaction and the free stream velocity). Other dynamical phenomena also take place in the recirculation bubble. The shear layer, bounding the upper part of the bubble, is subjected to two instabilities of medium characteristic frequencies as in subsonic separated flows [4] [17]. The shear layer is submitted to a convective instability leading to a vortex shedding at a Strouhal number around $S_L = \frac{fL}{U_e} \simeq 0.6 - 0.8$ expressed here as a Strouhal number based on the recir-

*Present address: Institut Aérotechnique, CNAM, 15 Rue Marat, 78210 Saint-Cyr-l'École, France

†Present address: Université Paris-Saclay, CNRS, CentraleSupélec, Laboratoire EM2C, 91190, Gif-sur-Yvette, France.

culation bubble length (L). It is also submitted to an absolute instability called "flapping" of the shear layer that has the characteristic frequency $S_L = \frac{fL}{U_e} \simeq 0.12 - 0.15$. This flapping consists in successive enlargment and shrinkage of the recirculation bubble. The shrinkage is associated to a vortex shedding downstream of the recirculation bubble. For supersonic flows, a low frequency flapping mode is also observed at a Strouhal number of $S_L = \frac{fL}{U_e} \simeq 0.03 - 0.04$ [20] [11]. In the following, we will refer to this low frequency mode as the "breathing" of the separated zone. In the same low frequency range $S_L = \frac{fL}{U_e} \simeq 0.03 - 0.04$, it is well established that the separation bubble and the system of shock waves (reflected and reattachment shock waves) are subjected to low frequency longitudinal oscillations called "the unsteadiness" of the SWBLI. This oscillatory motion can spread over several tenth of the boundary layer thickness. The SWBLI unsteadiness stresses solid structures to low frequency oscillating loads that can lead to damages of these structures, and therefore needs a very careful attention. Even if this phenomenon is well known, the related mechanisms are still not well understood.

Several explanations of the physical mechanisms responsible for the SWBLI have been proposed in the litterature. These mechanisms can be coarsly classified in two main categories [10].

The first mechanism consists in the excitation of the whole SWBLI by large scale coherent structures present within the incoming turbulent boundary layer and flowing through the interaction region with a caracteristic frequency corresponding to the low frequency SWBLI unsteadiness [13, 15, 14]. A second kind of mechanism has also been introduced in the literature, for which the dynamics of the recirculation bubble must be related to the unsteadiness of the whole SWBLI system and in particular to the reflected shock wave oscillations [21, 20, 30, 22, 1, 23].

Despite arguments in favor of each mechanism, no definitive explanation have yet been provided. Some authors argue that both mechanisms are at play in the onset of the SWBLI unsteadiness but the influence of the first mechanism decreases as far as the strength of the interaction decreases ([28] [6]).

In additions to these two main families of mechanims, a third kind of model have been introduced in the literature. It accounts for the incoming turbulence without requiring the existence of superstructures. [31] proposed a quantitative model involving the incoming boundary layer disturbrances in which the shock wave / separation bubble system is seen as a black-box filter/amplifier converting incoherent background disturbances into the observed spectra. This model only requires very low amplitude background disturbances in the flow that do not need to be in the form of coherent structures. Nevertheless, this model have the major drawback of not explaining the causes of the SWBLI unsteadiness. The relevance of this model have been strengthened by [25] who reproduced numerically the SWBLI unsteadiness (in particular the low frequency oscillations of the separation point) by forcing a 2D shock wave laminar boundary layer interaction (SWLBLI) with white noise.

The aim of the present work is to perform well resolved DNS of SWBLISs and analyse results in order to contribute to a better understanding of the SWBLI unsteadiness and the physical mechanism causing these low frequency oscillations. To this end, the canonical configuration of an oblique shock wave impinging a boundary layer developing on a flat plate is considered.

In order to better understand the mechanisms leading to the SWBLI unsteadiness, we first chose to perform a SWBLI simulation suppressing one of the two suspected mechanisms leading to the unsteadiness. By simulating the interaction between a laminar boundary layer and a incident shock wave (SWLBLI), we suppress the suspected influence of the large turbulent structures of the boundary layer on the SWBLI unsteadiness. The only remaining suspected cause of unsteadiness would be the dynamics of the separation bubble. The simulation of a SWTBLI is then undertaken. The dynamics of theses two flows are studied by mean of statistical an spectral analysis. A proper orthogonal analysis of the interaction zone is performed for the SWTBLI simulation that helps to understand the low frequency dynamics of this flow.

2. NUMERICAL METHODS.

We consider the compressible Navier-Stokes equations. The simulations are performed with an in-house parallel (MPI) Finite-Volume based DNS/LES solver developed at LIMSI-CNRS. The convective fluxes are discretized by Monotonicity-Preserving shock-capturing scheme (OSMP7), based on the Lax-Wendroff approach to obtain a 7^{th}-order accurate coupled time and space approximation. A 2^{nd}-order centered scheme is used for the diffusive fluxes [7]. The ability of this code to compute high Reynolds compressible (turbulent and shocked) flows has already been demonstrated in a previous work [24].

3. UNSTEADY SHOCK WAVE *LAMINAR* BOUNDARY LAYER INTERACTION (SWLBLI).

As a first step, by simulating the interaction between a laminar boundary layer and an incident shock wave, we suppress the suspected influence of the large turbulent structures of the boundary layer on the unsteadiness of the whole shock-wave/separation bubble system. The only remaining suspected cause of unsteadiness would be the dynamics of the separation bubble.

The flow conditions are similar to the test case of Degrez [9] ($M = 2.15$) with a shock wave angle increased up to 33.8° in order to strengthen the interaction and trigger the unsteadiness of the separation bubble.

The inlet boundary layer is created at the inlet of the domain thanks to a 4^{th} order polynomial approximation of a Blasius profile [12]. No-slip wall and adiabatic wall conditions are prescribed at the flat plate location ($y = 0$). Outlet time dependent non-reflecting boundary conditions [29] are imposed at the top surface and at the downstream outlet boundary of the computational domain. Periodic conditions are used in the spanwise direction (z). The shock wave is created at the top boundary by using the Rankine-Hugoniot relationships.

The domain is discretized using a cartesian mesh with non uniform spacing in the direction normal to the wall (y). The mesh size employs $400 \times 102 \times 200$ grid points in $(x \times y \times z)$. In the normal to the wall direction, the mesh is tightened close to the wall using a hyperbolic tangent law.

A snapshot of the flow is shown in figure 2. The discriminant criterion, introduced in [5] already used by [21] in the context of SWTBLI simulations, is used to identify the vortex structures present in the flow. Vortices are identified as regions in which the local topology of the streamlines is focal as defined in [5]. The discriminant is positive in these regions. In figure 2, the vortical structures are highlighted by plotting the isosurfaces of $\frac{\Delta}{(U_\infty/\theta)^6} = 10^{-12}$, where Δ is the discriminent and θ is the momentum thickness of the incoming boundary layer at the inlet of the simulation domain. These isosurfaces are colored by the magnitude of the longitudinal velocity. The shock waves are highlighted by isosurfaces of $\mid \nabla P \mid$ colored in grey.

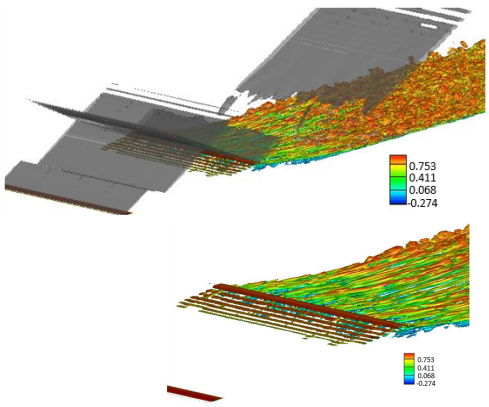

Figure 2: Up: Discriminent criterion ($\frac{\Delta}{(U_\infty/\theta)^6} = 10^{-12}$) colored by the magnitude of the longitudinal component of the velocity scaled by U_∞. Shock waves are highlighted by isosurfaces of $\mid \nabla P \mid$. Bottom: Discriminent criterion. Zoom around the separation bubble.

Large spanwise vortices, corresponding to the Kelvin-Helmholtz rolls that progressively develop, are clearly visible in the shear layer edging the recirculation bubble between the reflected and the incident shocks. After the incident shock impingement, the shear layer is populated by elongated structures in the streamwise direction that form hairpin like vortices characteristic of a turbulent boundary layer downstream of the reattachment. In the recirculation bubble, 3D structures are visible in the downstream part of the separation zone. Nevertheless, no coherent structures are visible in the early part of the interaction. The dynamical activity inside the recirculation bubble seems to be mainly concentrated in the second part of the separation.

Several probes have been located in the flow along lines in the spanwise direction. The locations of these probes in the plane $(\mathbf{x}, \mathbf{y})$ are shown in figure 3.

Probes 1 ($x/\delta = 18.75$, $y/\delta = 0.31$) and 4 ($x/\delta = 81.25$, $y/\delta = 0.31$) are located in the recirculation bubble, respectively in the early part and latter part of the separation. Probes 2 and 3 are located in the shear layer bounding the recirculation bubble. Probe 2 is located upstream of the incident shock wave impingement ($x/\delta = 50$, $y/\delta = 3.84$) whereas probe 3 is located downstream of the incident shock wave impingement ($x/\delta = 81.25$, $y/\delta = 0.93$). Finally, probe 5 have been located close to the wall just downstream of the reattachment of the boundary layer ($x/\delta = 92.5, y/\delta = 0.31$). For each probe location in the plane $(\mathbf{x}, \mathbf{y})$, the signal of any quantity corresponds to it spanwise averaged value. Moreover, the quantities have been recorded during around ten low frequency unsteadiness cycles.

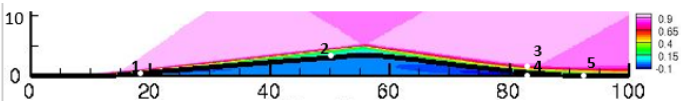

Figure 3: Time mean longitudinal velocity field averaged in the spanwise direction. The black line shows the isocontour $u = 0$. The velocitiy is scaled using U_∞ and the spatial coordinates are scaled using δ. Position of the probes.

The power spectral density of the longitudinal velocity signals for the probes 1 and 4 are shown in figure 4 with respect to the Strouhal number based on the separation lengh $S_L = \frac{fU_\infty}{L}$. The amplitude of the spectrum at probe 1 is about 50 times smaller than for probe 4. It confirms the observation made in figure 2 that the dynamical activity inside the recirculation bubble is mainly concentrated in the second part of the separation. The characteristic frequencies characterizing the dynamics inside the recirculation bubble are in agreement with the characteristic frequencies of the recirculation bubble and its shear layer

introduced above. At probe 1, the spectrum is dominated by low frequencies in the range $S_L \simeq 0.01 - 0.05$ characteristic of the breathing of the recirculation bubble. A second frequency packet at $S_L \simeq 0.11 - 0.15$ corresponds to the medium frequency flapping of the shear layer. The spectrum at probe 4 is also characterized by low ($S_L \simeq 0.01 - 0.05$) and medium frequencies $S_L \simeq 0.15$. Moreover, higher frequencies $S_L \simeq 0.5 - 0.6$, characteristic of the vortex shedding from the shear layer are present in the spectrum at probe 4.

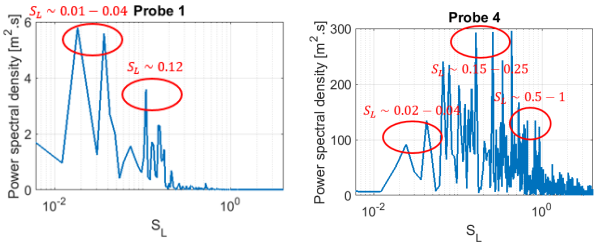

Figure 4: Premultiplied power spectral density of the longitudinal velocity component. Left: probe 1. Right: probe 4.

The power spectral density of the longitudinal velocity signals for the probes 2 and 3 are shown in figure 5 with respect to the Strouhal number based on the separation lengh $S_L = \frac{fU_\infty}{L}$. It allows to compare the characteristic frequencies of the shear layer before and after the incident shock wave impingement. The spectrum at probe 2 (before the incident shock wave) shows an activity of the shear layer at low frequencies ($S_L \simeq 0.01 - 0.03$) characteristic of the breathing of the separation bubble and medium frequencies ($S_L \simeq 0.15$) characteristic of the medium frequency flapping. The frequencies characterizing the vortex shedding from the shear layer ($S_L \simeq 0.5 - 0.6$) seems to be present in the spectrum but at a much lower amplitude. At probe 3, the amplitude of the spectrum are much larger than at probe 2. It shows that the dynamics of the shear layer is much more intense in the latter part of the separation zone. The characteristic frequencies of the low and medium frequency flapping of the shear layer are present in the spectrum. Moreover, higher frequencies around $St_L \simeq 3$ characterizing the vortex shedding are present in the spectrum with high amplitude. The same characteristic frequency ($St \simeq 3$) has also been recorded for the Kelvin-Helmholtz instabilities in a large separation at a blunt flat plate leading edge [8].

The power spectral density of the longitudinal velocity signal for probe 5 is shown in figure 6 with respect to the Strouhal number based on the separation lengh $S_L = \frac{fU_\infty}{L}$. The dynamics is characterized by almost the sames frequency ranges than at probe 3 with an increased intensity.

The study of the spectra of the longitudinal velocity at probes located in the interaction zone shows that the low

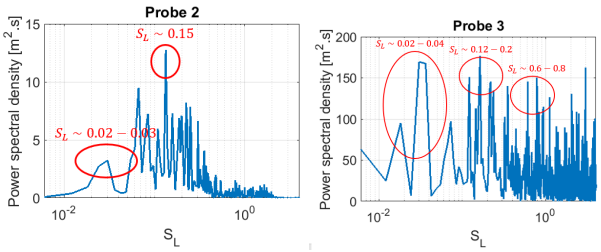

Figure 5: Premultiplied power spectral density of the longitudinal velocity component. Left: probe 2. Right: probe 3.

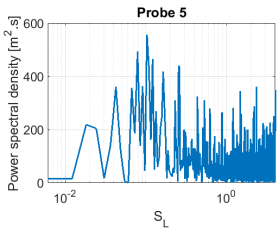

Figure 6: Premultiplied power spectral density of the longitudinal velocity component at probe 5.

frequency range characteristic of the SWBLI unsteadiness ($S_L \simeq 0.03 - 0.04$) is present in all the interaction zone. Moreover, the velocity fluctuations in the shear layer are characteristic from the flapping. Besides, the dynamics is much more intense in the latter part of the separation zone with the apparition of higher frequencies characteristic of the vortex shedding.

Regarding the separation and the reattachment points, we show the history of the mean value in the spanwise direction of the abscissa along the plate in figure 7. These abscissa are computed regarding the skin friction value (null or changing sign for two consecutive mesh points in the streamwise direction). We clearly see that, after a transient period where the location moves rapidly upstream, the separation point remains at a fixed position along the flat plate (figure 7-left). The history of the location along the flat plate of the foot of the reflected shock wave is plotted in figure 8. The foot of the shock wave is identified at each time of acquisition as the abscissa where the wall pressure becomes 20% bigger than P_∞. The reflected shock wave location along the flat plate remains constant versus time. Consequently, the SWBLI unsteadiness, characterized among other by the oscillations of the reflected shock wave and the separation point is not observed in our DNS of a SWLBLI. Nevertheless, we see in figure 7-right that the reattachment point is submitted to an oscillatory motion.

To find out the characteristic frequencies at which the reattachment point moves, we computed its power spectral density shown in figure 9. A first low frequency peak is visible at a Strouhal number $S_L = \frac{f_1 L}{U_e} \simeq 0.04$ charac-

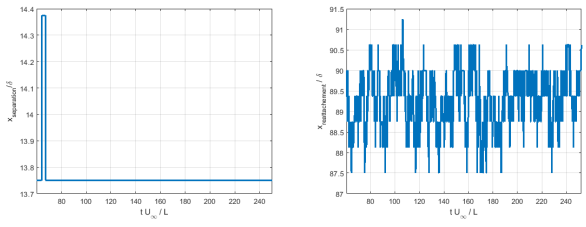

Figure 7: History of the mean location in the spanwise direction of the abscissa along the flat plate of the separation point, on the left, and the reattachment point, on the right.

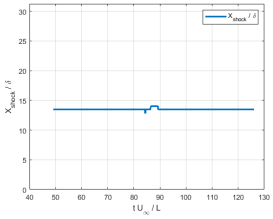

Figure 8: History of the mean location in the spanwise direction of the abscissa along the flat plate of the reflected shock foot.

teristic of the breathing of the separation bubble. We observe a second peak at a Strouhal of $S_L = \frac{f_2 L}{U_e} \simeq 0.145$ characteristic of the flapping of the shear layer. Further peaks around $S_L = \frac{f_3 L}{U_e} \simeq 0.6$ appear, that can be related to the shedding mode of this shear layer. The power spectrum of the location of the reattachment point clearly exhibits the generally admitted values of a separated boundary layer dynamics. Even if the dynamics of the separation bubble is well recovered, no unsteadiness of the whole SWBLI system is recorded and only the motion of the reattachment shock is observed. Obviously, this shock motion is linked to the reattachment movement.

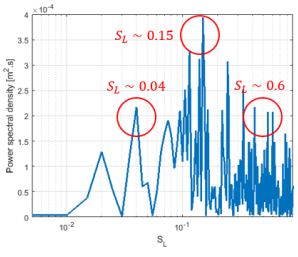

Figure 9: Premultiplied power spectral density of the reattachment point abscissa along the flat plate

This study of the laminar interaction shows that the low frequency activity characteristic of the breathing of the separation zone exist in the recirculation bubble. All the frequency information is found in the separation bubble, emitted from the reattachment point, and it even reaches the separation shock. However, the back flow in the bubble seems to damp those oscillations out so that they are not strong enough to make the reflected shock move. The SWBLI unsteadiness is therefore not observed in this case.

4. SHOCK WAVE TURBULENT BOUNDARY LAYER INTERACTION (SWTBLI)

The concluding remarks of the precedent paragrarph could suggest that the low-frequency oscillations found in the turbulent case is related to the presence of vortical structures upstream of the interaction. In order to confirm this analysis, DNS on a turbulent case have then been performed. In this context, the Synthetic Eddy Method (SEM), initially developed by Jarrin et. al. [16], was adapted to the compressible case. This method allows to create a realistic turbulent boundary layer as the inlet plane [24]. A compressible turbulent boundary layer have been generated using the synthetic inlet conditions. The flow conditions ($M_\infty = 2.33$, $Re_\theta = 2538.78$) are taken from [19] where a method is developed to trip an incoming laminar boundary layer and to obtain a turbulent boundary layer. We employ $800 \times 320 \times 120$ grid points in $(x \times y \times z)$. In the normal to the wall direction, the mesh is tightened close to the wall using a hyperbolic tangent law to ensure that the first $y^+ = 0.8$. The domain extent is $60.4\delta \times 16.7\delta \times 3.0\delta$ where δ is the inlet boundary layer thickeness.

As for the laminar interaction, several probes have been located in the interaction zone. The spectral analysis of the velocity signal, not presented in this paper, can be foud in [3]. It shows that the dynamics of the simulated SWTBLI exhibits most of the characteristic features already identified in the litterature. In particular, the shear layer surrounding the separation bubble is submitted to low frequency and medium frequency flapping associated to a vortex shedding in the downstream boundary layer. The dynamics of the early part of the interaction exhibits lower characteristic frequencies than the remaining of the interaction zone.

Histories of the separation and reattachment point abscissa averaged in the spanwise direction (respectively x_s and x_r) are plotted in figure 10. x_s corresponds to the most upstream abscissa at which the skin friction coefficient becomes negative. x_r corresponds to the most downtream abscissa at which the skin friction coefficient becomes positive again. The amplitude of the reattachment point motion is significantly larger than the amplitude of the separation point motion. This is in accordance with results obtained by other authors ([21], [2]). The power spectral densities of these two signals have been computed and are shown in figure 11. The reat-

tachment point is dominated by frequencies characteristic of the medium frequency ($S_L \simeq 0.15$) and low frequency ($S_L \simeq 0.03-0.05$) flapping of the shear layer, the medium frequency being more energetic. The motion of the separation point is dominated by the low frequency activity of the recirculation bubble and is characterized by the presence of very low frequency activity ($S_L \simeq 0.015$).
The separation length L variation with time has a standard deviation of $0.25L$. In the laminar case, the standard deviation is $0.0093L$. The flapping intensity relatively to the separation size is therefore much bigger in the turbulent case than in the laminar case.

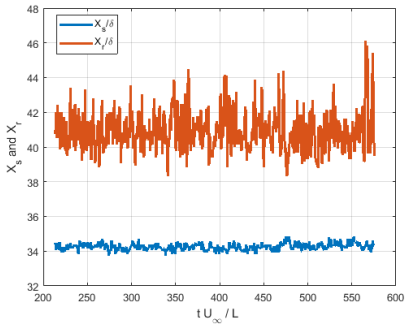

Figure 10: Time history of the spanwise averaged locations of the separation point $x_s(t)$ and the reattachment point $x_r(t)$

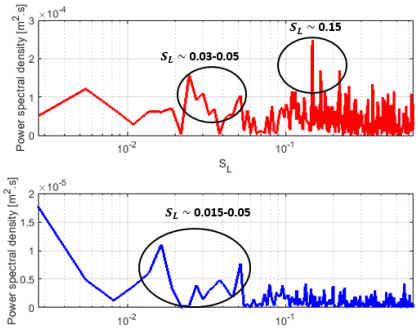

Figure 11: Power spectral density of the time history of the spanwise averaged location of the separation point $x_s(t)$ (red) and the time history of the spanwise averaged location of the reattachment point $x_r(t)$ (blue).

Figure 12 shows the history of the separation point location along the flat plate and the history of the position of the reflected shock waves foot X_{shock}. As in [2], the position of the shock wave is identified at each time of acquisition as the abscissa for which the wall pressure becomes 30% bigger than P_∞. The standard deviation of X_{shock} is 0.16δ. The covariance of $X_s(t)$ and $X_{shock}(t)$ is shown in figure 13 highlighting the high correlation between the motions of the separation point and the reflected shock wave.

These results show that the medium and low frequency

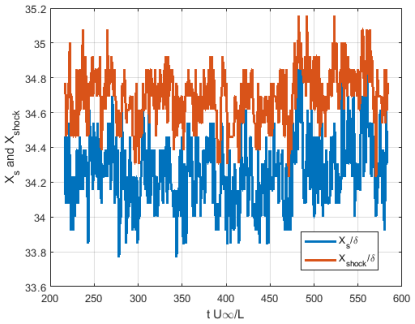

Figure 12: Time history of the spanwise averaged location of the separation point $x_s(t)$ and the reflected shock foot $X_{shock}(t)$.

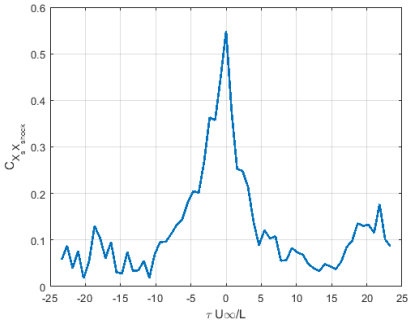

Figure 13: Distribution of the covariance between $x_s(t)$ and $X_{shock}(t)$ as a function of the non dimensionalized time lag $\tau U_\infty / L$.

of the recirculation bubble is recovered by our simulation, associated to the low frequency unsteadiness of the reflected shock wave.

The probability density function of $Cf = 0$ averaged in the spanwise direction (hereafter noted $PDF(Cf = 0)$) in the interaction region is shown in figure 14. The mean separation abscissa ($\bar{x}_s/\delta = 34.25$) and the mean reattachment abscissa ($\bar{x}_r/\delta = 40.9$) are reported by vertical lines. The increase of $PDF(Cf = 0)$ upstream of $\bar{x}_s$ is sharper than its decrease downstream of $\bar{x}_r$. It is coherent with the observation made in figure 10 that the amplitude of the motion of the reattachment point is significantly larger than the amplitude of the motion of the separation point.
Moreover, the progressive increase (respectively decrease) of $PDF(Cf = 0)$ upstream of $\bar{x}_s$ (respectively downstream of $\bar{x}_r$) highlights the irregular amplitude of the separation (respectively reattachment) point oscillations that are submitted to temporal modulations. The modulation of the reattachment point oscillations are larger than the separation points oscillations.
The history of the skin friction averaged in the spanwise direction at $x = \bar{x}_s$ (respectively $x = \bar{x}_r$) is plotted in figure 15-top-left (respectively 15-top-right). The time av-

erage interval dt between two consecutive sign changes (Cf becoming negative) at $x = \overline{x}_s$ is $dtU_\infty/\overline{L} \simeq 4.1$, that corresponds to a frequency of $S_L \simeq 0.24$. At $x = \overline{x}_r$, we have $dtU_\infty/\overline{L} \simeq 9.1$ that corresponds to a frequency of $S_L \simeq 0.11$. Therefore, the sign change of the spanwise averaged skin friction coefficient at $x = \overline{x}_s$ and $x = \overline{x}_r$ occurs at frequencies more or less in the range of the characteristic frequency of the medium frequency flapping of the recirculation bubble. The probability of a change in the sign of Cf upstream of $x = \overline{x}_s$ is lower than at $x = \overline{x}_s$. The frequency of such a sign change is then lower. For example, the history of the skin friction averaged in the spanwise direction at $x/\delta = 34$ is plotted in figure 15-bottom-left. At this abscissa, the frequency of the change of the sign of Cf is $S_L \simeq 0.05$. Similarly, the probability of a change in the sign of Cf downstream of $x = \overline{x}_r$ is lower than at $x = \overline{x}_r$. The history of the skin friction averaged in the spanwise direction at $x/\delta = 42.75$ is plotted in figure 15-bottom-right. At this abscissa (downstream of $x = \overline{x}_r$), the frequency of the change of the sign of Cf is $S_L \simeq 0.03$.

The changes of the sign of the spanwise average skin friction coefficient upstream (respectively downstream) of the mean separation point (respectively reattachment point) therefore occurs at lower frequencies than near the mean separation point (respectively mean reattachment point). At the two selected abscissa, this low frequency falls in the characteristic range of the low frequency flapping of the recirculation bubble. These low frequency change of sign of the skin friction upstream (respectively downstream) of the mean separation (respectively reattachment) point corresponds to large displacements of the separation (respectively reattachment) point occuring at low frequency.

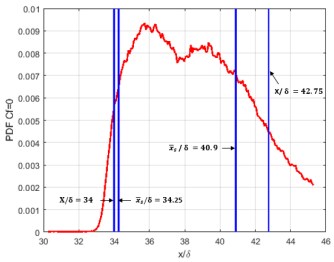

Figure 14: Probability density function of $Cf = 0$ averaged in the spanwise direction

In order to get more insight in the low frequency dynamics of the SWTBLI, a proper orthogonal decomposition (POD) has been applied to the velocity ($\mathbf{u} = (u,v,w)^T$) and pressure (p) fields in a subdomain bounding the interaction zone. POD is a method of data analysis that allows to obtain low dimensional approximate descriptions of high-dimensional processes. It is widely used for data processing and has first been used by [18] to identify coherent structures in turbulent flows. Any scalar

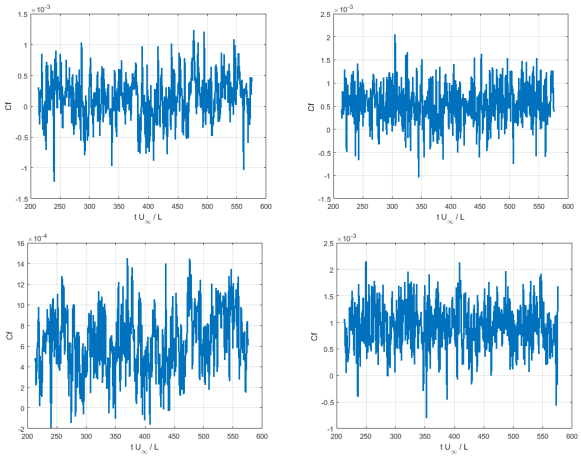

Figure 15: History of the skin friction averaged in the spanwise direction at 4 abscissa in the interaction region. The 4 abscissa are highlighted by vertical lines in figure 14. Up left: $x/\delta = 34.25$ (mean separation point). Up right: $x/\delta = 40.9$ (mean reattachment point). Bottom left: $x/\delta = 34.0$. Bottom right: $x/\delta = 42.75$.

(respectively vectorial) physical quantity $q(x,y,z,t)$ can be decomposed in scalar (respectively vectorial) spatial modes $\Phi^m(x,y,z)$ sorted by decaying energy ($\int_x\int_y\int_z(\Phi^m)^2 dxdydz > \int_x\int_y\int_z(\Phi^{m+1})^2 dxdydz \quad \forall \quad m \geq 1$):

$$q(x,y,z,t) = \sum_{m\geq 1} \alpha^m(t)\Phi^m(x,y,z), \tag{1}$$

where α^m is the temporal coefficient representing the amplitude of the m^{th} mode.

In our study, this decomposition is obtained using the snapshot POD technique [27] in which the temporal coefficients are obtained by solving the following eigenvalue problem:

$$\sum_{t'} C_{tt'}\alpha^m(t') = \lambda^m\alpha^m(t), \tag{2}$$

where the temporal correlation tensor writes $C_{tt'} = \int_x\int_y\int_z q(x,y,z,t).q(x,y,z,t')dxdydz$. with "." denoting a scalar product. The Euclidian scalar product is used in our study. Each eigen value λ^m represents the energy of the m^{th} mode.

The spatial modes Φ^m are computed by projecting the realizations ($q(x,y,z,t)$) onto the temporal coefficients : $\Phi^m(x,y,z) = \sum_t q(x,y,z,t)\alpha^m(t)$. The spectral density of the POD energy contained in a set of modes Υ is defined as $\varpi(\Upsilon) = \sum_{m\in\Upsilon}\lambda^m \mid \widehat{\alpha}^m(f) \mid^2$ where $\widehat{\alpha}^m(f)$ is the Fourier transform of α^m.

The method of snapshots was used with 361 fields with a time separation of $0.192\frac{L}{U_\infty}$. The time interval between the first and the last snapshot corresponds to about 2.5 low frequency SWTBLI unsteadiness periods and about 7 periods of the medium frequency flapping of the recir-

culation bubble. The POD is applied on the whole part of the fields; in other words, the analysis is not conducted on the fluctuating fields after the time mean is substracted, as often employed. Then, the first POD mode is supposed to be representative of the time average of the field. In the following, the fluctuating modes refer to the modes m higher than 1 ($m > 1$).
The average value of the power spectral density of α^m over two distinct sets of modes is plotted (for the first 29 fluctuating modes ($2 \leq m \leq 30$) (blue) and for the remaining modes ($m > 30$) (red)) in figure 16-left for the velocity field, and figure 17-left for the pressure field. The spectral density of the POD energy is plotted in figure 16-right respectively 17-right for the velocity field, respectively the pressure field (for the first 29 fluctuating modes ($2 \leq m \leq 30$) (blue) and for the remaining modes ($m > 30$) (red)).

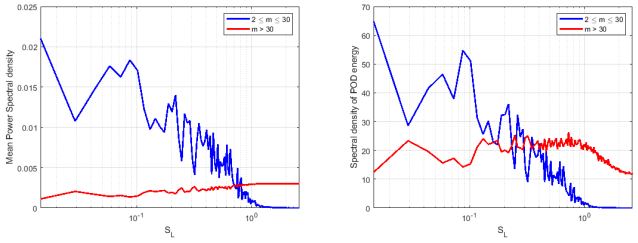

Figure 16: Left: average of the power spectral density of α^m over two distinct sets of modes for the POD on the velocity field. Right: spectral density of POD energy for two distinct sets of modes for the POD on the velocity field.

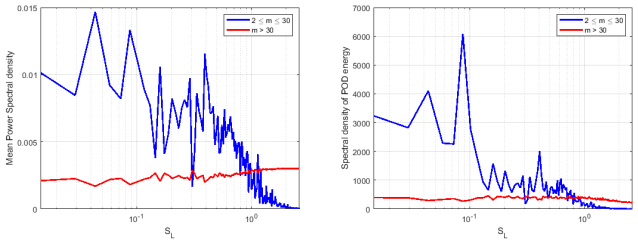

Figure 17: Left: average of the power spectral density of α^m over two distinct sets of modes for the POD on the pressure field . Right: spectral density of POD energy for two distinct sets of modes for the POD on the pressure field.

Figures 16 and 17 show that the low frequency activity of the flow is mostly contained in the first 29 fluctuating both for the velocity field and on the pressure field. In order to get more insight in the low frequency dynamics of the flow, especially in the range of frequency of the SWTBLI unsteadiness, we reconstructed the time evolution of the velocity and of the pressure fields using only the first 30 POD modes as follows:

$$q_r(x,y,z,t) = \sum_{m=1}^{30} \alpha^m(t)\Phi^m(x,y,z) \qquad (3)$$

where q_r is the reconstructed field (velocity or pressure field).

The reconstruction obtained have then been averaged in the homogeneous spanwise direction in order to simplify the dynamical interpretation. This simplification is acceptable as the broadband low frequency unsteadiness of the interaction zone has been shown to be predominantly two-dimensional [22, 26].

The analysis of the evolution of the reconstructed fields (not shown here but presented in [3]) confirms the low/medium frequency dynamical features evoked above (breathing and flapping of the recirculation bubble, low frequency oscillations of the reflected shock wave).

When looking at animations of the reconstructed flow (not shown here), one can see that the dynamic of the flow is dominated by the medium frequency flapping of the recirculation bubble. This dominant dynamic feature of the reconstructed flow corresponds to cycles of enlargment and shrinkage of the separation bubble. The phase of enlargment corresponds to a motion of the reflected shock wave in the upstream direction (in phase with the motion of the separation point as shown in figure 13). The shrinkage phase is accompanied with a shedding of a large amount of fluid from the recirculation zone.

A sequence of visualizations of the reconstructed longitudinal velocity averaged in the spanwise direction at time intervals of $11L/U_\infty$ (corresponding to a frequency of sampling of $S_L \simeq 0.09$) is shown in figure 18. These visualization correspond to the maximum extent of the recirculation bubble for five successive medium frequency flapping cycles. These visualizations highlight the irregularity of the flapping patterns at the medium frequency. Indeed visible discrepancies are visible between the size of the recirculation bubble (maximum size of the cycle) for these consecutive flapping cycles. This irregularity of the medium frequency flapping can be related to the irregularities highlighted in the amplitudes of the separation and reattachment point oscillations, already mentionned in figures 14 and 15, that were found to introduce low frequencies in the characteristic range of the breathing of the separation bubble ($S_L \simeq 0.03$).

5. CONCLUSIONS AND PERSPECTIVES

The direct numerical a SWLBLI and a SWTBLI have been performed. The analysis of the dynamics of the flows has been undertaken in order to contribute to a better understanding of the SWBLI unsteadiness.

The results tend to show that the SWTBLI unsteadiness is related to the dynamics of the separation bubble.

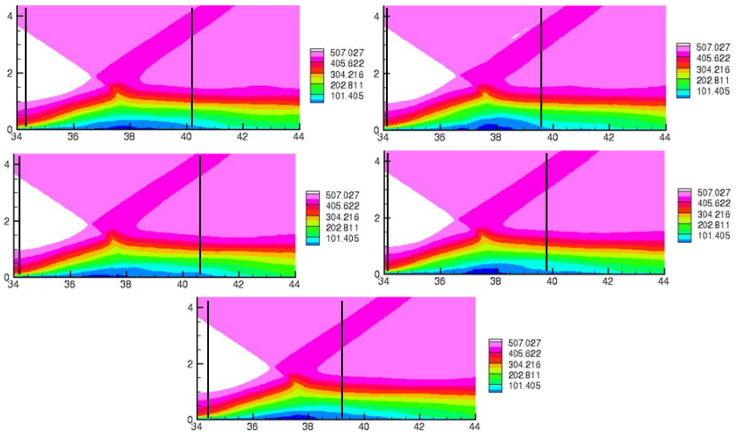

Figure 18: Sequence of visualizations of the reconstructed longitudinal velocity field at different times (from left to right and up to bottom). Black vertical lines show the position of x_s and x_r.

The dynamics appears to be dominated by the medium frequency flapping ($S_L \simeq 0.12 - 0.15$). The amplitude of this medium frenquency flapping have been shown to be irregular in time, the maximum size of the recirculation bubble being submitted to modulations between successive cycles. This behaviour of the separation bubble is responsible for the low frequency temporal modulation of the separation and reattachment points motion amplitude, related to the breathing of the separation bubble ($S_L \simeq 0.03 - 0.04$). The reflected shock wave appears to be forced by the separation point motion, and hence being submitted to a low frequency oscillatory motion.

The same dynamical behaviour of the recirculation bubble is at play in the SWLBLI where the low frequency activity characteristic of the breathing of the separation zone exist in the recirculation bubble, emitted from the reattachment point, and even reaching the foot of the separation shock. However, in the laminar case, the back flow in the bubble seems to damp those oscillations out so that they are not strong enough to make the separation point (and consequently the reflected shock) move.

Two concomitant explanations can be put forward to explain the differences between the laminar and the turbulent cases :

- in the turbulent case, the incoming turbulent structures excite the separation point. This perturbation is sufficient to trigger the motion of separation point submitted to the low frequency oscillations emitted at the reattachment point related to the breathing.

- in the turbulent case, the recirculation bubble is fully turbulent. The separated zone (and particularly the subsonic zone) is much smaller than in the laminar case. The damping of the low frequency signal emitted at the reattachment point is therefore largely lower than in the laminar case. Moreover, in the laminar case, the transition to turbulence is triggered by the incident shock impingement upon the shear layer and the transition to turbulence occurs only in the latter part of the recirculation bubble. Consequently, the shedding intensity is much lower than in the turbulent case relatively to the size of the recirculation bubble.

In order to stregthen the validity of the presented results, new simulations of the same interactions have been performed using finner meshes and a larger physical time of simulation. The analyses of the dynamics have been deepened using spectral proper orthogonal decomposition in order to be able to clearly associate spatial modes with given frequencies. These results will be published in coming papers.

REFERENCES

[1] G. Aubard, X. Gloerfelt, and J.-C. Robinet. Large-eddy simulation of broadband unsteadiness in a shock/boundary-layer interaction. *AIAA Journal*, 51:2395–2409, 2013.

[2] Guillaume Aubard. *Large Eddy Simulation of the low-frequency unsteadiness of a shock-wave turbulent boundary layer interaction on a flat plate*. Theses, Arts et Métiers ParisTech, June 2012.

[3] Ismaïl Ben Hassan Saïdi. *Numerical simulations of the shock wave-boundary layer interactions*. Theses, Université Paris-Saclay, November 2019.

[4] R. Cherry, N. J.; Hillier and M. E. M. P. Latour. Unsteady measurements in a separated and reattaching flow. *Journal of Fluid Mechanics*, 144:13–46, 1984.

[5] Min S Chong, Julio Soria, AE Perry, J Chacin, BJ Cantwell, and Y Na. Turbulence structures of wall-bounded shear flows found using dns data. *Journal of Fluid Mechanics*, 357:225–247, 1998.

[6] N. T. Clemens and V. Narayanaswamy. Low-Frequency Unsteadiness of Shock Wave/Turbulent Boundary Layer Interactions. *Annual Review of Fluid Mechanics*, 46:469–492, 2014.

[7] V. Daru and C. Tenaud. High order one-step monotonicity-preserving schemes for unsteady compressible flow calculations. *Journal of Computational Physics*, 193(2):563 – 594, 2004.

[8] Ph. Debesse, L. Pastur, F. Lusseyran, Y. Fraigneau, C. Tenaud, C. Bonamy, A. V. G. Gavalieri, and P. Jordan. A comparison of data reduction techniques for the aeroacoustics analysis of flow over a blunt flat plate. *Theoretical and Computational Fluid Dynamics*, 30:253–274, 2016.

[9] G. Degrez, C. H. Boccadoro, and J. F. Wendt. The interaction of an oblique shock wave with a laminar boundary layer revisited. An experimental and numerical study. *Journal of fluid mechanics*, 177(13):247–263, 1987.

[10] J. Delery. Some physical aspects of shock wave/boundary layer interactions. *Shock Waves*, 19(6):453–468, 2009.

[11] P. Dupont, S. Piponniau, A. Sidorenko, and J. François Debiève. Investigation of an oblique shock reflection with separation by piv measurements. In *Proceedings of the 45th AIAA Aerospace Sciences Meeting and Exhibit*, 2007.

[12] Guillaume Fournier, A Chpoun, Yann Fraigneau, and Christian Tenaud. Direct numerical simulations of the shock-induced separation of a laminar boundary layer. In *Direct and Large-Eddy Simulation 10, Limasol ,Cyprus*, 2015.

[13] B. Ganapathisubramani, N. T. Clemens, and D. S. Dolling. Planar imaging measurements to study the effect of spanwise structure of upstream turbulent boundary layer on shock induced separation. In *Proceedings of the 44th AIAA Aerospace Sciences Meeting and Exhibit*, page 324, 2006.

[14] Bharathram Ganapathisubramani, Noel Clemens, and David Dolling. Effects of upstream coherent structures on low-frequency motion of shock-induced turbulent separation. In *45th AIAA Aerospace Sciences Meeting and Exhibit*, page 1141, 2007.

[15] Bharathram Ganapathisubramani, NT Clemens, and DS Dolling. Effects of upstream boundary layer on the unsteadiness of shock-induced separation. *Journal of fluid Mechanics*, 585:369–394, 2007.

[16] N. Jarrin, S. Benhamadouche, D. Laurence, and R. Prosser. A synthetic-eddy-method for generating inflow conditions for large-eddy simulation. *International Journal of Heat and Fluid Flow*, 27(4):585–593, 2006.

[17] M. Kiya and K. Sasaki. Structure of large-scale vortices and unsteady reverse flow in the reattaching zone of a turbulent separation bubble. *Journal of Fluid Mechanics*, 154:463–491, 1985.

[18] JL Lumley. Atmospheric turbulence and wave propagation. the structure of inhomogeneous turbulence. *AM Yaglom et VI Tatarski*, page 166–178, 1967.

[19] Nathan J Mullenix, Datta V Gaitonde, and Miguel R Visbal. Spatially developing supersonic turbulent boundary layer with a body-force-based method. *AIAA journal*, 51(8):1805–1819, 2013.

[20] S. Piponniau, J. P. Dussauge, J. F. Debiève, and P. Dupont. A simple model for low-frequency unsteadiness in shock-induced separation. *Journal of Fluid Mechanics*, 629:87–108, 2009.

[21] S. Pirozzoli and F. Grasso. Direct numerical simulation of impinging shock wave/turbulent boundary layer interaction at M=2.25. *Physics of Fluids*, 18(6):065113, 2006.

[22] Stephan Priebe and M Pino Martín. Low-frequency unsteadiness in shock wave–turbulent boundary layer interaction. *Journal of Fluid Mechanics*, 699:1–49, 2012.

[23] Stephan Priebe, Jonathan H Tu, Clarence W Rowley, and M Pino Martín. Low-frequency dynamics in a shock-induced separated flow. *Journal of Fluid Mechanics*, 807:441–477, 2016.

[24] Ismaïl Ben Hassan Saïdi, Guillaume Fournier, and Christian Tenaud. On the behaviour of high-order one-step monotonicity-preserving scheme for direct numerical simulation of shocked turbulent flows. *International Journal of Computational Fluid Dynamics*, 34(9):671–704, 2020.

[25] A Sansica, ND Sandham, and Z Hu. Forced response of a laminar shock-induced separation bubble. *Physics of fluids*, 26(9):093601, 2014.

[26] Kenzo Sasaki, Diogo C Barros, André VG Cavalieri, and Lionel Larchevêque. Causality in the shock wave/turbulent boundary layer interaction. *arXiv preprint arXiv:2012.03285*, 2020.

[27] L. Sirovich. Turbulence and the dynamics of coherent structures. i. coherent structures. *Quarterly of applied mathematics*, 45(3):561–571, 1987.

[28] L. Souverein, P. Dupont, J. F. Debiève, J.-F. Dussauge, B. van Oudheusden, and F. Scarano. Effect of interaction strength on the unsteady behavior of shock wave boundary layer interactions. In *Prodeedings of the 39th AIAA Fluid Dynamics Conference*, page 3715, 2009.

[29] K.W. Thompson. Time Dependent Boundary Conditions for Hyperbolic Systems. *Journal of computational physics*, 68(1):1–24, 1987.

[30] E. Touber and N. D. Sandham. Large-eddy simulation of low-frequency unsteadiness in a turbulent shock-induced separation bubble. *Theoretical and computational fluid dynamics*, 23(2):79–107, 2009.

[31] E. Touber and N. D. Sandham. Low-order stochastic modelling of low-frequency motions in reflected shock-wave/boundary-layer interactions. *Journal of Fluid Mechanics*, 671:417?465, 2011.